High-field magnetization of $KEr(MoO_4)_2$

K. Kutko,[1] B. Bernáth,[2,3] V. Khrustalyov,[1] O. Young,[2,3] H. Engelkamp,[2,3] P. C. M. Christianen,[2,3] L. Prodan,[4] Y. Skourski,[5] L. V. Pourovskii,[6,7] S. Khmelevskyi,[8] and D. Kamenskyi[4,9,10,*]

[1]*B. Verkin Institute for Low Temperature Physics and Engineering of the National Academy of Sciences of Ukraine (ILTPE), Nauky Avenue 47, Kharkiv 61103, Ukraine*

[2]*High Field Magnet Laboratory (HFML - EMFL) Radboud University Toernooiveld 7, NL-6525 ED Nijmegen, The Netherlands*

[3]*Institute for Molecules and Materials, Radboud University, Heyendaalseweg 135, NL-525 AJ Nijmegen, The Netherlands*

[4]*Experimental Physics V, Center for Electronic Correlations and Magnetism, Institute of Physics, University of Augsburg, D-86159 Augsburg, Germany*

[5]*Dresden High Magnetic Field Laboratory (HLD-EMFL), Helmholtz-Zentrum Dresden–Rossendorf, D-01328 Dresden, Germany*

[6]*CPHT (Centre de Physique Théorique), CNRS, Ecole Polytechnique, Institut Polytechnique de Paris, Route de Saclay, F-91128 Palaiseau, France*

[7]*Collège de France, Université PSL, 11 place Marcelin Berthelot, F-75005 Paris, France*

[8]*Research Center for Materials Science and Engineering, Vienna University of Technology, Karlsplatz 13, A-1040 Vienna, Austria*

[9]*Department of Physics, Humboldt-Universitat zu Berlin, Newtonstrasse 15, D-12489 Berlin, Germany*

[10]*German Aerospace Center (DLR), Institute of Optical Sensor Systems, Rutherfordstrasse 2, D-12489 Berlin, Germany*

(Received 19 July 2023; revised 9 October 2023; accepted 5 December 2023; published 30 January 2024)

We report a magnetization study of the rare-earth-based paramagnet $KEr(MoO_4)_2$ in a magnetic field up to 50 T. A recent observation of massive magnetostriction and rotational magnetocaloric effects in this compound triggered interest in the microscopic mechanism behind these phenomena. We combine several experimental techniques to investigate the magnetization behavior up to its saturation along three main crystallographic directions. The synergy of magnetic torque measurements and vibrating sample magnetometry allowed us to reconstruct parallel and perpendicular components of the magnetization vector, enabling us to trace its evolution up to 30 T. Our experiments reveal the magnetization saturation along all principle axes well below the value, expected from crystal electric field calculations. We argue that an externally applied magnetic field induces a distortion of the local environment of Er^{3+} ions and affects its crystal electric field splitting.

DOI: 10.1103/PhysRevB.109.024438

I. INTRODUCTION

The magnetostrictive materials exhibit a strain caused by an externally applied magnetic field. Particularly strong magnetostriction has been reported in a magnetically ordered state [1,2]. Recently, we reported a remarkably strong magnetostrictive response of the insulator paramagnet $KEr(MoO_4)_2$ [3]. The magnetoelastic strain observed in $KEr(MoO_4)_2$ ($\sim 6\times10^{-4}$) exceeds the strain value reported for other rare-earth paramagnetic oxides by one order of magnitude, and reaches a value typical for metallic antiferromagnets, such as NdB_6 or $ErGa_2$ [4]. Such a high lattice sensitivity to the applied magnetic field together with a giant rotational magnetocaloric effect reported in this compound earlier [5] provide great perspectives for applications in cryogenic and magnetic technologies [6].

Our previous analysis revealed a strong coupling between the magnetic Er^{3+} ions and the crystal lattice via quadrupolar moments of Er^{3+} [3]. The key role of quadrupolar moments and its interactions in rare-earth-based paramagnets was earlier shown for RVO_4 (R = Ho, Tb, Dy, Er) compounds with a tetragonal zirconia structure [7–9]. Here, we aim for a further understanding of the microscopic mechanism of magnetostriction in $KEr(MoO_4)_2$ via a comprehensive experimental study of the magnetization process supported by *ab initio* calculations [10]. We find that the lattice distortion induced by the external magnetic field is so strong that the conventional crystal electric field (CEF) approach is insufficient to simultaneously describe the magnetization and magnetostriction curves of $KEr(MoO_4)_2$.

We employed a number of experimental techniques: Superconducting quantum interference device (SQUID) magnetometry, inductive magnetization measurements in pulsed magnetic fields up to 50 T, vibrating sample magnetometry (VSM), and torque measurements in a 33-T Bitter magnet. The combination of these techniques allows to reconstruct the magnetic field behavior of the parallel and perpendicular components ($M_\parallel$ and $M_\perp$) as well as spatial orientation of the Er^{3+} magnetic moment.

Single crystals of $KEr(MoO_4)_2$ have been grown by the flux method at the Institute for Low Temperature Physics in Kharkiv, Ukraine. To confirm the quality of the samples used in our study, we performed a compositional analysis using scanning electron microscopy in combination with energy-dispersive x-ray spectroscopy and elemental mapping. This analysis revealed the stoichiometric chemical composition and homogeneous distribution of Er and K atoms in our crystal. All samples used for experiments reported in this

*dmytro.kamenskyi@physik.uni-augsburg.de

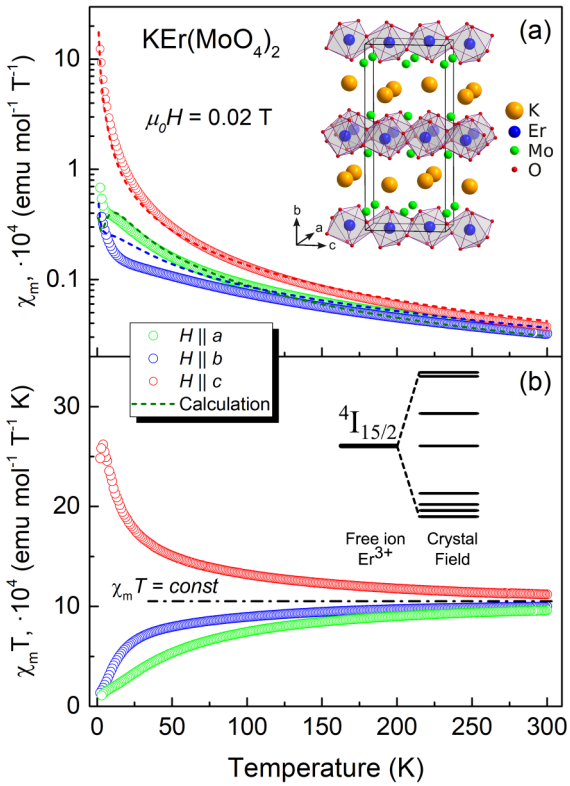

FIG. 1. (a) The molar magnetic susceptibility χ_m of $KEr(MoO_4)_2$ along the a, b, and c directions at $\mu_0 H = 0.02$ T. Symbols represent the experimental data, and the dashed lines show the susceptibility calculated by the exact diagonalization of the CEF Hamiltonian in the magnetic field. The inset displays the crystallographic structure of $KEr(MoO_4)_2$. (b) Curves $\chi_m T$ are shown to illustrate the deviation of the magnetic susceptibility from Curie law ($\chi_m T = \text{const}$ in the Curie model). The inset shows the splitting of the Er^{3+} multiplet $^4I_{15/2}$ into eight Kramers doublets by CEF.

paper were cleaved from the same bulk crystal. Samples of the same origin were used for the magnetostriction study [3].

$KEr(MoO_4)_2$ crystallizes as light pink transparent plates with the D_{2h}^{14} ($Pbcn$) orthorhombic space group ($a = 5.06$ Å, $b = 18.23$ Å, and $c = 7.92$ Å) [11] [see the inset in Fig. 1(a)]. Er^{3+} ions are located in an octahedral oxygen environment, which generates a CEF and lifts the degeneracy of the lowest Er^{3+} multiplet $^4I_{15/2}$ into eight Kramer's doublets with a gap between the lowest and highest states of 39.1 meV (454 K or 315 cm^{-1}, respectively) [see the inset in Fig. 1(b)] [3,12,13]. The energy gaps between the lowest doublet, the first, and the second excited doublets are 1.6 and 3.9 meV (19.5 and 45.3 K, or 13 and 31.5 cm^{-1}). These states are further split by an externally applied magnetic field (due to the Zeeman effect). The small energy gaps between the levels of the $^4I_{15/2}$ multiplet together with the sensitivity of the lattice to the magnetic field, leads to an anomalous behavior of the magnetization, which we evaluate further in this paper.

II. RESULTS AND DISCUSSION

Figure 1(a) shows the molar magnetic susceptibility χ_m of $KEr(MoO_4)_2$ measured by SQUID magnetometry along the a, b, and c crystallographic directions in the external magnetic field of $\mu_0 H = 0.02$ T. It reveals a strongly anisotropic paramagnetic behavior with the easy axis along the c direction. In $KEr(MoO_4)_2$, the interaction of $4f$ electrons with the CEF is smaller than the spin-orbit coupling, which is typical for comparable $4f$ compounds [14]. Consequently, there is no quenching of the orbital momentum and the ground state contains significant spin and orbital contributions which result in a large anisotropy. Another consequence of the small CEF is energy gaps between the lowest-energy levels of the Er^{3+} multiplet (1.6 and 3.9 meV, with temperature equivalents 19.5 and 45.3 K, respectively) which is significantly below room temperature. This makes the magnetic moment of an individual Er^{3+} ion temperature dependent. Thus, Curie and Curie-Weiss models, developed for magnetic systems composed of particles with a temperature- and field-independent magnetic moment, cannot be applied to this compound. In Fig. 1(b), we illustrate the deviation of the magnetic susceptibility in $KEr(MoO_4)_2$ from the Curie law by plotting the $\chi_m T$ product, which is supposed to be a constant if the Curie law obeys. One can see a significant deviation from the linearity over the entire temperature range. Consequently, determination of the g factors, Curie constants, and the effective magnetic moment from the Curie-Weiss law would not provide adequate values. Note that the same restriction for the use of the Curie-Weiss law applies for all magnetic systems where the contribution of the higher-energy levels is significant. To evaluate the measured susceptibility $KEr(MoO_4)_2$, it is necessary to take into account the contribution of the whole multiplet. To first order, the susceptibility measured in a static field is $\chi_m = M_\parallel/H$ and the contribution of all levels of the $^4I_{15/2}$ multiplet is given by the equation which accounts for the thermal population of the excited states [15]:

$$M_\parallel = \frac{N_A g \mu_B \sum_{i=0}^{7} m_{\pm i} e^{-(E_i + g m_{\pm i} \mu_B H)/kT}}{\sum_{i=0}^{7} e^{-(E_i + g m_{\pm i} \mu_B H)/kT}}. \quad (1)$$

Here, i is an index designating the energy level and E_i is the separation of the ith level from the ground state ($i = 0$, $E_0 = 0$). μ_B is the Bohr magneton, k is the Boltzmann constant, N_A is Avogadro's number, g is the Landé factor of the spectroscopic splitting, $g = 6/5$ for the Er^{3+} ion, and T is the sample temperature. $m_{\pm i}$ denotes the field projection of the total angular momentum of individual states ($\pm$ states for the upper and lower branches of Kramers doublets).

Equation (1) is widely used for describing the magnetic susceptibility and magnetization of compounds containing d-type transition ions [15] where the initial CEF splitting is an order of magnitude exceeding the Zeeman energy. However, for the f ions the CEF splitting is comparable to the Zeeman energy which leads to the magnetic field dependence of the states' wave functions. Thus, the Van Vleck susceptibility [16], which accounts for quadratic contributions of the magnetic field to energy levels, has to be considered. The dashed lines in Fig. 1(a) show the magnetic susceptibility of $KEr(MoO_4)_2$ calculated by diagonalization of the CEF Hamiltonian in the magnetic field taking into account the Van Vleck terms. The CEF parameters was obtained by an *ab initio* method [10] and given in the Ref. [3].

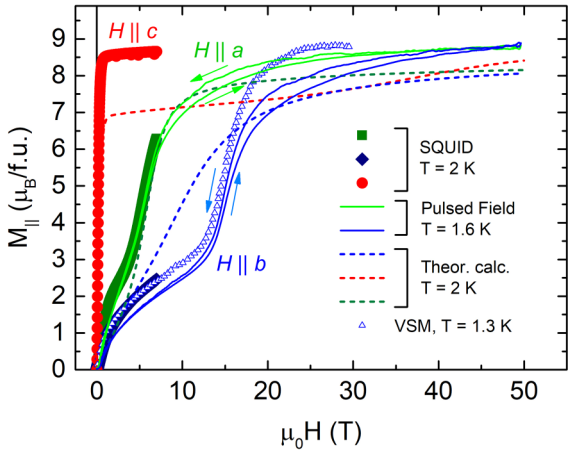

FIG. 2. The field dependencies of the parallel component of the magnetization of $KEr(MoO_4)_2$ measured by SQUID at $T = 2$ K (solid symbols), VSM at 1.3 K (open symbols), and in pulsed magnetic fields (solid lines). Dashed lines display the result of calculations based on CEF parameters obtained by the *ab initio* calculations described in Ref. [3]. Results for the different crystallographic directions are denoted by the red ($H \parallel c$), green ($H \parallel a$), and blue ($H \parallel b$) symbols and lines.

The Van Vleck term manifests also in the magnetization process. In Van Vleck's magnets the magnetization evolves via two processes. In small fields and low temperatures, the magnetization grows quite rapidly with the applied field due to the Zeeman splitting of the lowest Kramers doublet and reaches a quasisaturation when the Zeeman splitting of the $m_{\pm 0}$ levels exceeds the thermal energy (in a few tesla). As the magnetic field grows further, $m_{\pm 0}$ grows as well, until it reaches its maximal value ($m = 15/2$) which happens when the Zeeman energy exceeds the energy of the CEF (significantly above a hundred tesla).

Figure 2 displays the magnetization curves measured by SQUID magnetometry (solid symbols), VSM in a Bitter 33-T magnet (open symbols), and the inductive method in pulsed magnetic fields (solid lines). A significant magnetocaloric effect and short pulse duration (25 ms full pulse, upraise 7 ms, $T = 1.6$ K at $B = 0$ before the pulse) makes curves measured in pulsed magnetic fields smoother than curves measured in the Bitter magnet. The core difference between the static and pulsed field experiments is the fact that the pulse duration (1–100 ms) sets nearly adiabatic conditions for the sample, which is opposite to a static field environment, where isothermal conditions can be ensured. If the sample demonstrates a significant magnetocaloric effect, that could lead to a substantial difference between magnetization curves (or other thermodynamic properties) measured in static and pulsed fields (see, for example, Fig. 3 in Ref. [17]). Adiabaticity itself should not lead to irreversibility or looping of the measured curve. However, in the case of a massive magnetocaloric effect some heat is transferred from the sample to the environment (or otherwise, as the effect can be negative as well) thus the return temperature path will be not preserved. In fact, the pulsed magnetization curves are rather adiabatic than isothermic and the difference between up and down curves of the pulse field measurements is due to irreversible heat transfer between the sample and the environment.

When the magnetic field is along the easy axis (c axis), the magnetization saturates at 1.1 T, and reaches a value of $8.6\mu_B/Er^{3+}$, which is close to the expected saturation value for free Er^{3+} ion of $9\mu_B/Er^{3+}$. For a magnetic field applied along a and b axes, the magnetization exhibits an abrupt enhancement at 5.7 and 14.5 T and saturation at about 25 and 40 T, respectively. Our previous study reveals that the feature in the magnetization curve at 14.5 T for $H \parallel b$ is related to the massive magnetostriction effect [3]. The dashed lines in Fig. 2 display the magnetization calculated based on the CEF parameters obtained using an *ab initio* method reported in Ref. [3]. For all crystallographic directions, these calculated magnetization curves initially grow up to about $7\mu_B/Er^{3+}$ after which they exhibit a slow enhancement without ever approaching the expected saturation value even up to 50 T. In contrast, we experimentally observe the saturation below 40 T, even for the hard b-axis. Thus, in contrast to RVO_4 compounds, where the CEF approximation is sufficient to describe the magnetization behavior [7] in $KEr(MoO_4)_2$ there is another additional mechanism responsible for the earlier saturation of the magnetization.

As we mentioned above, the $^4I_{15/2}$ multiplet of Er^{3+} is split by the crystal field into 8 Kramers doublets spread over an energy interval of 39.1 meV. The exact arrangement of those states is determined by CEF effects. The CEF splitting and wave functions of the $^4I_{15/2}$ multiplet in $KEr(MoO_4)_2$ were calculated in Ref. [3] obtaining a good quantitative agreement for the overall splitting and the CEF level structure. These wave functions can be written as superpositions $\sum \alpha_m |m\rangle$ of the total-angular-momentum eigenstates $|m\rangle \equiv |J = 15/2; m\rangle$ for the moment projections $m = \pm 1/2, \pm 3/2, \ldots, \pm 13/2, \pm 15/2$ along a given quantization axis. A low-symmetry environment with large CEF mixing leads to contributions of any eigenstate $|m\rangle$ being spread over many CEF states. In particular, the eigenstates $|m = \pm 15/2\rangle$ corresponding to a fully saturated moment along the a crystallographic axis were found to contribute to both the CEF ground state and the highest-energy excited one (see the Supplemental Material of Ref. [3]). On the other hand, the saturation of the magnetization along the a axis seen in Fig. 2 above 20 T implies that the ground state wave function at such fields contains only an $m = 15/2$ component, thus seemingly suggesting the Zeeman energy being essentially larger than the total CEF splitting ~40 meV. However, taking into account that for Er^{3+} $g = 6/5$, such a magnitude of the Zeeman energy would require a magnetic field significantly above 100 T, which contradicts the experimental results. The same argument holds for the hard b axis, where the saturated-moment eigenstate can be again shown to be spread over all the CEF levels, but for which an essentially full saturation is observed in Fig. 2 at about 40 T.

These findings indicate that in order to achieve an agreement between theory and experiments a modification of the CEF is essential. However, with the adjustments of the CEF parameters we may improve the situation for the particular crystallographic direction with controversial results for other axes in return. Based on the previous analysis, we conclude that the earlier reported lattice deformation [3] in

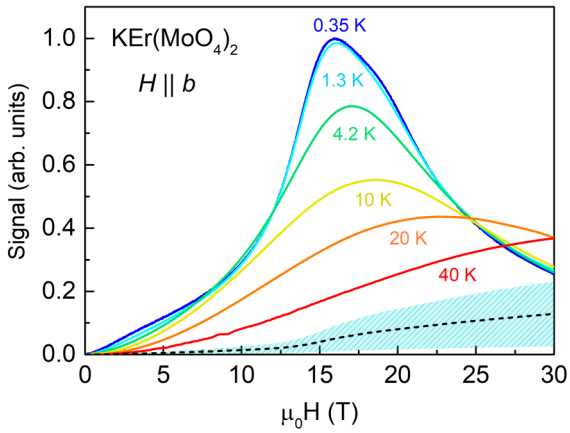

FIG. 3. Magnetic torque curves of $KEr(MoO_4)_2$ measured at different temperatures. The dashed line and blue shade show the torque signal that is caused by the shape of the sample.

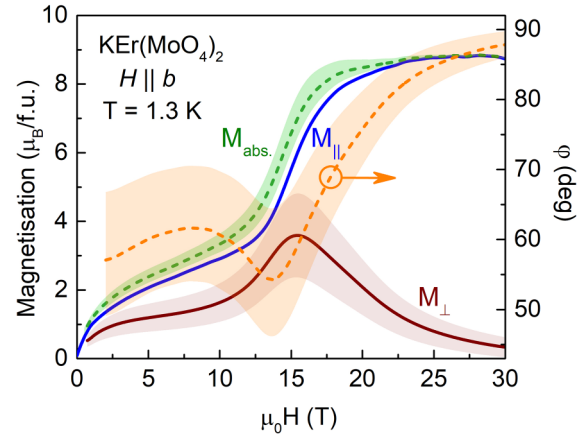

FIG. 4. The calculated absolute value of the magnetization of $KEr(MoO_4)_2$ (dashed green line) and its parallel (solid blue) and perpendicular (solid brown) components. Measurements are done with the magnetic field applied along the b axis at 1.3 K. Orange dashed line shows the orientation of the magnetization in the bc plane (right scale). $\phi = 0$ corresponds to $M \parallel c$. The blur around the curves shows confidence interval (see text for the details).

$KEr(MoO_4)_2$ significantly affects the octahedral oxygen environment of the Er^{3+} ions. The deformation of the local environment, in turn via the CEF, modifies the electronic wave functions in such a way that the lowest-energy $^4I_{15/2}$ state morphs into a pure saturated-moment eigenstate $|m = \pm 15/2\rangle$ much more rapidly than one would expect from the zero-field CEF splitting. Indeed, as seen in Fig. 2, the theoretical magnetization curves calculated from the zero-field CEF exhibit a much slower approach to the saturation value. In our experiment, the field effect upon CEF manifests itself as an enhancement of the magnetization between 5 and 10 T for the a axis and between 15 and 20 T for the b axis. At higher fields, the lattice distortion becomes even stronger and affects the anisotropy of the system. Above 30 T the ground state wave function becomes an essentially pure $|m = \pm 15/2\rangle$ state.

To complete the experimental investigation of the magnetization process along the hard b axis, we evaluate the spatial orientation of the magnetization using VSM and magnetic torque measurements. The torque measurements were performed on a plate-shaped specimen of size $0.500 \times 0.516 \times 0.062$ mm (ac plate) using a piezocantilever. The sample was mounted such that its crystallographic a axis was parallel to the longest side of the cantilever plate and the b axis is perpendicular to the cantilever plate. The signal measured by the cantilever is linearly proportional to the applied torque, τ. As we demonstrate later this signal is approximately proportional to the magnetization component perpendicular to the magnetic field ($M_\perp$). Figure 3 displays the temperature evolution of the τ signal. At lowest temperatures, it exhibits peculiarities in the field similar to magnetization. With increasing temperature the thermal fluctuations between the low-lying CEF states cause additional mixing of the electronic states which makes the magnetic field effect less pronounced and anomalies in the field behavior tend to vanish.

When the applied magnetic field $\mathbf{H}$ is perpendicular to the cantilever, the sample with magnetization $\mathbf{M}$ experiences a torque,

$$\tau = \nabla(\mathbf{M} \cdot \mathbf{H}) \times \mathbf{d} + \mathbf{H} \times \mathbf{M}, \qquad (2)$$

where $\mathbf{d}$ is the distance from the sample to the torque axis. The first term in Eq. (2) arises from the isotropic magnetization of the sample and induces a torque in a magnetic field gradient. In our experiments, we took great care of precisely positioning the sample in the field center of the Bitter magnet such that $\nabla\mathbf{H} \approx \mathbf{0}$ and the first term is negligible (for more details, see Refs. [18,19]). Thus, the measured signal is due to the second term which originates from the anisotropy of the magnetization when $\mathbf{H} \times \mathbf{M} \neq \mathbf{0}$. It is important to note that there are two sources of such anisotropy: (i) the single-ion anisotropy of the Er^{3+} ion τ_A and (ii) the shape anisotropy of the sample τ_S. In our experimental geometry both these forces act in the same direction, inducing a torque which rotates the sample towards an orientation with the magnetic field in the ac plane.

The first contribution $\tau_A = HM \sin\theta$, where θ is the angle between $\mathbf{H}$ and $\mathbf{M}$. Thus, by dividing τ_A by the magnetic field, we obtain $M_\perp = M \sin\theta$ in arbitrary units. The τ_S induced by the shape anisotropy is a monotonic function of the applied field and sample magnetization, so $\tau_S \propto MH$.

As we see in Fig. 3, the torque signal exhibits a broad maximum at about 15.5 T and decays when the magnetization saturates and $M_\perp \to 0$. However, even at 30 T, when the magnetization is almost saturated τ is far from zero. We assume that a significant part of the measured signal is due to the shape contribution τ_S. The dashed line in Fig. 3 shows an expected shape contribution to the τ. In order to obtain the field dependence of $M_\perp$ we subtract this τ_S from τ and got $M_\perp$ in arbitrary units. Based on the magnetostriction results [3], we assumed that the absolute magnetization M_{abs} reaches saturation at about 20 T, and taking absolute numbers for $M_\parallel$ from the VSM result we rescaled the perpendicular magnetization curve accordingly to get the absolute value, $M_{\text{abs}} = |\mathbf{M}|$.

Figure 4 shows the parallel and perpendicular components of the magnetization together with its absolute value and the orientation with respect to the c axis at 1.3 K and $H \parallel b$. The solid blue curve displays $M_\parallel$, measured by VSM [18,19].

$M_\perp$ was obtained from the torque measurements as described above and shown in Fig. 4 by the brown line. The blur around the brown curve shows the confidence interval based on the uncertainty of the shape contribution to the τ. These data allowed us to reconstruct an absolute value of the magnetization vector M_{abs} (dashed green curve) and its orientation (dashed orange curve). The magnetization vector is always in the plane between the magnetic easy axis c and the applied magnetic field, which in our case is the bc plane. Results of the calculation depend on the saturation field of M_{abs} which we guessed from the magnetostriction curve and from the contribution of τ_S in the torque signal. The blur of the curves in Fig. 4 shows the confidence interval of the M_{abs} saturation between 19 and 20 T.

At small fields, both $M_\perp$ and $M_\parallel$ increase with increasing magnetic field (shown in Fig. 4 with blue and brown solid lines, respectively). Due to the enhancement of the magnetic energy the moment rotates towards the b axis along the field. In higher magnetic fields, however, the lattice deformation becomes so strong that it changes not only the magnetic moment but also the anisotropy of the system. As one can see in Fig. 4, above 10 T while M_{abs} continues to grow, the magnetic moment rotates back towards the c axis. Above 17 T, M_{abs} is almost saturated, $M_\perp$ decays, and the further magnetization process is an alignment of the magnetic moment along the magnetic field (the rotational process).

III. SUMMARY

We performed a detailed study of the magnetization process of $KEr(MoO_4)_2$ in magnetic fields up to 50 T. We demonstrate that for samples with high single-ion anisotropy, a combination of VSM and torque measurements, performed in a well-chosen geometry, allows for the reconstruction of the absolute value of magnetization and its spatial orientation. Using the pulsed magnetic fields we determined a saturation field along the b axis (hard direction) of 40 T which is an order of magnitude below the value expected from the CEF splitting of the Er^{3+} multiplet $^4I_{15/2}$. We found that by the adjustments of the CEF parameters we may improve results for the particular magnetic field direction, however, with controversial results for other axes.

We reveal the distortion of the local environment of the Er^{3+} ions by a magnetic field applied along the crystallographic b axis. Via CEF, this distortion leads to a wave-function and magnetic anisotropy modification which in turn triggers anomalies in the magnetization and magnetostriction curves.

For a complete reconstruction of the ground state wavefunction evolution, a few further steps have to be taken. Complementary to this study, it is essential to perform structural and spectroscopy measurements in magnetic fields above 15 T as well as magnetostriction measurements in the direction perpendicular to the applied magnetic field to determine all components of the magnetoelastic tensor. After this, CEF parameters could be determined with a higher precision based on the simultaneous analysis of the magnetic field splitting of the $^4I_{15/2}$ multiplet components, magnetization, and lattice deformation in high magnetic fields.

ACKNOWLEDGMENTS

This work was supported by HFML-RU and HLD at HZDR, members of the European Magnetic Field Laboratory (EMFL). This work is part of the research program of the Netherlands Organisation for Scientific Research (NWO). D.K. was supported by the PRIME program of the German Academic Exchange Service (DAAD) with funds from the German Federal Ministry of Education and Research (BMBF). B.B. acknowledges support by the European Research Council (Grant Agreement No. 835279-Catch-22). L.V.P. acknowledges support by the European Research Council Grant No. ERC-319286-"QMAC" and the computer team at CPHT. L.P. acknowledges the support by the Deutsche Forschungsgemeinschaft (DFG, German Research Foundation)–TRR 360–492547816.

K.K. and B.B. contributed equally to this work.

[1] J. Atulasimha and A. B. Flatau, A review of magnetostrictive iron–gallium alloys, Smart Mater. Struct. **20**, 043001 (2011).

[2] A. Miyata, H. Suwa, T. Nomura, L. Prodan, V. Felea, Y. Skourski, J. Deisenhofer, H.-A. Krug von Nidda, O. Portugall, S. Zherlitsyn, V. Tsurkan, J. Wosnitza, and A. Loidl, Spin-lattice coupling in a ferrimagnetic spinel: Exotic H-T phase diagram of $MnCr_2S_4$ up to 110 T, Phys. Rev. B **101**, 054432 (2020).

[3] B. Bernáth, K. Kutko, S. Wiedmann, O. Young, H. Engelkamp, P. C. M. Christianen, S. Poperezhai, L. V. Pourovskii, S. Khmelevskyi, and D. Kamenskyi, Massive magnetostriction of the paramagnetic insulator $KEr(MoO_4)_2$ via a single-ion effect, Adv. Electron. Mater. **8**, 2100770 (2022).

[4] M. Doerr, M. Rotter, and A. Lindbaum, Magnetostriction in rare-earth based antiferromagnets, Adv. Phys. **54**, 1 (2005).

[5] V. Tkáč, A. Orendáčová, E. Čižmár, M. Orendáč, A. Feher, and A. G. Anders, Giant reversible rotating cryomagnetocaloric effect in $KEr(MoO_4)_2$ induced by a crystal-field anisotropy, Phys. Rev. B **92**, 024406 (2015).

[6] É. Du Trémolet de Lacheisserie, *Magnetostriction: Theory and Applications of Magnetoelasticity* (CRC Press, Boca Raton, FL, 1993).

[7] P. Morin, J. Rouchy, and Z. Kazei, Magnetoelastic properties and level crossing in $HoVO_4$, Phys. Rev. B **51**, 15103 (1995).

[8] C. Detlefs, F. Duc, Z. A. Kazeĭ, J. Vanacken, P. Frings, W. Bras, J. E. Lorenzo, P. C. Canfield, and G. L. J. A. Rikken, Direct observation of the high magnetic field effect on the jahn-teller state in $TbVO_4$, Phys. Rev. Lett. **100**, 056405 (2008).

[9] Y. Hirano, S. Skanthakumar, C.-K. Loong, N. Wakabayashi, and L. A. Boatner, Lattice and magnetic properties of $ErVO_4$ and $ErPO_4$, Phys. Rev. B **66**, 024424 (2002).

[10] P. Delange, S. Biermann, T. Miyake, and L. Pourovskii, Crystal-field splittings in rare-earth-based hard magnets: An *ab initio* approach, Phys. Rev. B **96**, 155132 (2017).

[11] S. Chong, S. Perry, B. J. Riley and Z. J. Nelson, Crystal structures and comparisons of potassium rare-earth molybdates $KRE(MoO_4)_2$ (RE = Tb, Dy, Ho, Er, Yb, and Lu), Acta Crystallogr., Sec. E **76**, 1871 (2020).

[12] V. I. Kut'ko, Dynamics of layered Jahn–Teller crystals of rare-earth compounds (review), Fiz. Nizk. Temp. **31**, 3 (2005).

[13] S. Poperezhai, P. Gogoi, N. Zubenko, K. Kutko, V. I. Kutko, A. S. Kovalev, and D. Kamenskyi, Terahertz lattice dynamics of the potassium rare-earth binary molybdates, J. Phys.: Condens. Matter **29**, 095402 (2017).

[14] A. Abragam and B. Bleaney, *Electron Paramagnetic Resonance of Transition Ions* (Clarendon Press, Oxford, U.K., 1970), p. 43.

[15] J. C. Lashley, R. Stevens, M. K. Crawford, J. Boerio-Goates, B. F. Woodfield, Y. Qiu, J. W. Lynn, P. A. Goddard, and R. A. Fisher, Specific heat and magnetic susceptibility of the spinels $GeNi_2O_4$ and $GeCo_2O_4$, Phys. Rev. B **78**, 104406 (2008).

[16] J. H. Van Vleck, Quantum mechanics: The key to understanding magnetism, in *Nobel Lectures, Physics 1971–1980*, edited by S. Lundqvist (World Scientific, Singapore, 1992), p. 353.

[17] M. G. Zavareh, Y. Skourski, K. P. Skokov, D. Yu. Karpenkov, L. Zvyagina, A. Waske, D. Haskel, M. Zhernenkov, J. Wosnitza, and O. Gutfleisch, Direct measurement of the magnetocaloric effect in $La(Fe, Si, Co)_{13}$ compounds in pulsed magnetic fields, Phys. Rev. Appl. **8**, 014037 (2017).

[18] A. McCollam, P. G. van Rhee, J. Rook, E. Kampert, U. Zeitler, and J. C. Maan, High sensitivity magnetometer for measuring the isotropic and anisotropic magnetisation of small samples, Rev. Sci. Instrum. **82**, 053909 (2011).

[19] L. C. J. M. Peters, P. C. M. Christianen, H. Engelkamp, G. C. Groenenboom, J. C. Maan, E. Kampert, P. T. Tinnemans, A. E. Rowan, and U. Zeitler, Magnetic anisotropy of individually addressed spin states, Phys. Rev. Res. **3**, L042042 (2021).